LAWRENCE
LIVERMORE
NATIONAL
LABORATORY

LLNL-JRNL-808330

Rapid retreat of the southwestern Laurentide Ice Sheet driven by Bolling-Allerod warming

S. L. Norris, M. Margold, J. C. Gosse, A. J. Hidy, D. G. Froese

April 8, 2020

Geology

Disclaimer

Rapid retreat of the southwestern Laurentide Ice Sheet during the Bølling-Allerød interval

Sophie L. Norris[1,2*], Lev Tarasov[3], Alistair J. Monteath[1], John C. Gosse[2], Alan J. Hidy[4], Martin Margold[5] and Duane G. Froese[1]

[1] Department of Earth and Atmospheric Sciences, 1-26 Earth Sciences Building, University of Alberta, Edmonton, T6G 2E3, Alberta, Canada
[2] Department of Earth Sciences, Dalhousie University, 1355 Oxford Street, Halifax, B3H 4R2, Nova Scotia, Canada
[3]Department of Physics and Physical Oceanography, Memorial University of Newfoundland, St. John's, A1B 3X7, Newfoundland, Canada
[4]Centre for Accelerator Mass Spectrometry, Lawrence Livermore National Laboratory, 7000 East Avenue, Livermore, CA 94550, USA
[5] Department of Physical Geography and Geoecology, Charles University in Prague, Faculty of Science, Albertov 6, 128 43, Praha 2, Czech Republic

***Corresponding author: sophie.norris@dal.ca, duane.froese@ualberta.ca**

ABSTRACT

The timing of Laurentide Ice Sheet deglaciation along its southwestern margin controlled the evolution of large glacial lakes and has implications for human migration into the Americas. Accurate reconstruction of the ice sheet's retreat also constrains glacial isostatic adjustment models and is important for understanding ice-sheet sensitivity to climate forcing.

Despite its significance, retreat of the southwestern Laurentide Ice Sheet (SWLIS) is poorly constrained by minimum-limiting 14C data. We present 26 new cosmogenic 10Be exposure ages spanning the western Interior Plains, Canada. Using a Bayesian framework, we combine these data with geomorphic mapping, 10Be, and high-quality minimum-limiting 14C ages to provide an updated chronology. This dataset presents an internally consistent retreat record and indicates that the initial detachment of the SWLIS from its convergence with the Cordilleran

Ice Sheet began by ca. 15.0 ka, concurrent with or slightly prior to the onset of the Bølling-Allerød interval (14.7–12.9 ka) and retreated >1200 km to its Younger Dryas (YD) position in ~2500 yr. Ice-sheet stabilization at the Cree Lake Moraine facilitated a meltwater drainage route to the Arctic from glacial Lake Agassiz within the YD, but not necessarily at the beginning. Our record of deglaciation and new YD constraints demonstrate deglaciation of the Interior Plains was ~60% faster than suggested by minimum 14C constraints alone. Numerical modeling of this rapid retreat estimates a loss of ~3.7 m of sea-level equivalent from the SWLIS during the Bølling-Allerød interval.

INTRODUCTION

Deglaciation of the Laurentide Ice Sheet (LIS) was the dominant control on Late Glacial (ca. 15–11.6 ka) sea-level rise (Carlson and Clark, 2012; Clark and Tarasov, 2014). The LIS response to Northern Hemisphere warming during the Bølling-Allerød (B-A) interstadial (14.7–12.9 ka; Rasmussen et al., 2014) is of particular interest because it provides an assessment of ice-sheet sensitivity to millennial-scale climate change. Numerical modeling (Gregoire et al., 2012, 2016; Tarasov et al., 2012) indicates a collapse of the ice saddle that connected the Cordilleran Ice Sheet (CIS) and southwestern LIS (SWLIS) was concordant with B-A warming (ca. 14.5–12.9 ka). However, the rate of ice retreat and meltwater-equivalent contribution of the SWLIS during this period remains uncertain.

The existing deglaciation chronology for the SWLIS from Dyke et al. (2003), updated by Dalton et al. (2020), is based primarily on radiocarbon data. This has been problematic for the Interior Plains of Canada, where the earliest dates are associated with Quaternary vertebrates and limited by unquantified biases between ice retreat and colonization of the region by plants and animals

(cf. Froese et al., 2019). Within the SWLIS, luminescence dating and a small number of 10Be exposure ages have been used to complement 14C chronologies; however, no attempts have been made to construct a regional retreat chronology that combines these methods. The existing deglaciation chronology assumes ice-margin stabilization at the Cree Lake Moraine, a moraine system >1200 km northeast of the Last Glacial Maximum margin suspected to date to the Younger Dryas stadial (YD; 12.9–11.7 ka; Dyke et al., 2003). Yet, an absence of chronological control on this moraine system and large discrepancies between dating methods across the region mean the deglacial response of the SWLIS is poorly constrained.

We present 10Be exposure ages from glacial erratics spanning the western Interior Plains (Fig. 1). We combine the new chronology with geomorphic mapping and preexisting 10Be exposure (n = 12), luminescence (n = 41), and "high-quality" minimum-limiting 14C dates (n = 96) to determine the timing and rate of retreat (see the Supplemental Material1). We combine these data within a Bayesian framework and present a retreat record consistent across chronological methods. We then use numerical model simulations to estimate the rate of ice-volume loss and sea-level contribution from the SWLIS.

METHODS

We collected samples from 26 boulders for 10Be cosmogenic surface exposure dating at five locations. These included: four from the Pine Lake Moraine (PLM), six from gravel bars within the Beaver River Spillway, five from erosional residuals at the head of the Clearwater Lower Athabasca Spillway (CLAS), five from the Cree Lake Moraine (CLM), and six from the western and eastern parts of the upper Cree Lake Moraine (Fig. 1). All samples were processed in the CRISDal Lab, Dalhousie University (Halifax, Nova Scotia, Canada), and analyzed for 10Be/9Be

79 at the Center for Accelerator Mass Spectrometry, Lawrence Livermore National Laboratory
80 (Livermore, California, USA).
81
82 Dates are reported using the time-dependent CRONUS LSDn production-rate scaling of Lifton et
83 al. (2014) and the "primary" production rate of Borchers et al. (2016). We report exposure ages
84 with no correction for snow shielding or erosion. Glacial isostatic adjustment (GIA) affects the
85 elevation, and thus the 10Be concentration, of our samples. In this region, the majority of surface
86 rebound occurred shortly after ice retreat when our samples were at an elevation (~40 m) lower
87 than modern. Accordingly, we applied a GIA correction of 3%–8% to all 26 samples (see the
88 Supplemental Material).
89
90 We performed a $\chi 2$ test ($p = 0.05$) to confirm that dates from each sample site are normally
91 distributed, and use Chauvenet's criterion of exclusion to systemically identify outliers. We then
92 report error-weighted mean ages for each site. Internal age uncertainties were calculated as the
93 larger of the standard error of the weighted mean or weighted standard deviation. Total
94 uncertainties are reported by combining the internal error in quadrature with production-rate
95 uncertainty.
96
97 We combined our new 10Be exposure dates with a database of published luminescence (infrared
98 and optically stimulated luminescence), 10Be exposure, and recalibrated minimum-limiting 14C
99 chronologies. This database of "high-quality" dates excludes 14C dates on bulk sediments,
100 terrestrial shells, or mixed assemblages (see Table S3 in the Supplemental Material). We treated
101 the existing luminescence and 14C dates at the site level similar to the 10Be exposure data and

group sites from a single landform or dune field within ~40 km regions (see the Supplemental Material).

We integrated these chronological data within a Bayesian age model using OxCal version 4.4 (Bronk Ramsey, 2009). The model uses the known sequence of ice retreat, demarcated by recessional moraines, as a "prior model" and follows the transect of cosmogenic 10Be exposure dates from this study (Fig. 2).

We re-ran the best-fitting North American ice-sheet model simulations of Tarasov et al. (2012) with revised minimum-maximum isochrone nudging timing over the 21–9.28 ka interval consistent with our new ages. We used these new simulations to estimate the rate of ice-volume loss and equivalent sea-level contribution from the SWLIS (defined as 49°–60°N, 125°–105°W). The model includes 39 ensemble parameters that are calibrated to address uncertainties in climate forcing, basal drag, ice calving, and the amount of nudging toward the input target ice-margin chronologies. For each time step, the nudging adjusts surface mass balance (within physical uncertainties) for model grid cells that are inconsistent with the input target ice-margin minimum-maximum isochrones (interpolated between available time slices). We calculated the mean ice-retreat rate (Fig. 3) along transects taken at 100 km intervals perpendicular to ice retreat.

NEW ICE MARGIN RETREAT CHRONOLOGY

Initial ice sheet separation and ice margin retreat across the Interior Plains

Initial detachment of the southern LIS and CIS is reported at 14.9 ± 0.9 ka from 10Be exposure dates from the Foothills Erratics Train (Margold et al., 2019; site A in Figs. 1 and 3A).

Luminescence dates from this region (sites E–F; Table S3) show a wide distribution when individual ages are considered, but grouping ages regionally to within ~40 km provides a chronology consistent with the exposure dates (Fig. 2). Tightly clustered minimum 14C ages on ultrafiltered collagen from bones from the SWLIS periphery indicate deglaciation before ca. 13.8 ka (sites B–D; Table S3). Samples from the PLM yield ages ~6–8 ka younger than all other sites. We interpret erratics at this site to have been exhumed post-glacially and exclude them from further discussion. 10Be exposure dates indicate the margin retreated to the Beaver River region by 13.5 ± 0.8 ka (n = 6). Tightly clustered 14C dates between the Foothills Erratics Train and the Beaver River region record deglaciation prior to 13.3 ka, including ultrafiltered collagen dates from Edmonton (site N; Table S3), and luminescence records, though variable, support this chronology (sites O–Q; Table S3).

Our 10Be exposure dates indicate deglaciation of the CLAS region at 13.0 ± 1.1 ka (n = 4). These dates agree with luminescence dates to the northwest (sites Y–Z; Table S3). Minimum-limiting 14C dates are also consistent with deglaciation prior to ca. 12.6 ka. 10Be exposure dates from the CLM and western upper Clear Lake Moraine (UCLM-W) indicate moraine formation by 12.7 ± 0.9 ka (n = 5; excluding one outlier at 16.9 ± 0.3 ka) and 12.3 ± 0.9 ka (n = 3), respectively. In contrast, 14C dates in the same region, largely from basal lake sediments, indicate later deglaciation (ca. 10.7–10.3 ka; Dyke et al., 2003; Fisher et al., 2009; Dalton et al., 2020). However, in the context of older more-southerly 10Be exposure, luminescence, and 14C ages, these samples likely reflect the minimum-limiting nature of deglacial 14C dates. Therefore, we regard the CLM and UCLM-W as the YD position of the SWLIS. This moraine system extends >600 km and represents a significant stabilization of the LIS during the YD cold reversal. We cannot determine

whether recession and re-advance preceded the formation of the outer moraines of the UCLM-E at 11.2 ± 0.7 ka (n = 2; excluding one outlier at 16.0 ± 0.3 ka) or whether these moraines represent an ~1000 yr stillstand.

IMPLICATIONS

Opening of the deglacial ice free corridor

The rapid deglaciation of the SWLIS has implications for the biogeographic connections between Beringia and continental North America, including human migrations. The combined chronologies presented here indicate southern LIS–CIS detachment began at ca. 15 ka, with substantial retreat of the LIS and formation of a deglacial "ice-free corridor" after ca. 13.5 ka (Margold et al., 2019; Froese et al., 2019). This chronology does not support the open passage at 15 ka proposed by Potter et al. (2018). Their approach utilized 14C dates that have not been reproduced, and placed emphasis on isolated luminescence dates that fall outside site means considered here (cf. Froese et al., 2019). Likewise, the later opening hypothesized by Pedersen et al. (2016) based on dates from basal lake sediment is unlikely given our chronology, which places the LIS at the CLM position by ca. 13 ka. At present, the intermediate model by Heintzman et al. (2016), which uses 14C and paleogenetics of bison to argue for an ice-free corridor by 13.2 ka, is most consistent with our chronology.

Northwestern drainage of glacial Lake Agassiz

The timing of ice-free conditions in the CLAS provides a minimum estimate on the northwestern drainage of glacial Lake Agassiz. Geological interpretations in northern Alberta (Smith and Fisher, 1993), luminescence evidence from the Mackenzie River delta (Murton et al., 2010), and offshore

data in the Arctic Ocean (Condron and Winsor, 2012; Keigwin et al., 2018) propose the spillway constituted the northwestern outlet of Lake Agassiz during the YD (Teller et al., 2005). Our chronology supports this and implies the CLAS provided a viable link for the northwestern drainage of Lake Agassiz during the YD, but not necessarily at its beginning (cf. Young et al., 2020; Norris et al., 2021). This chronology is also consistent with the results of data-constrained glaciological modeling (Tarasov and Peltier, 2005) that found even without opening of northwestern drainage, mass loss from the Keewatin ice dome provided a meltwater flux during the YD. In the glaciological model simulation most consistent with our ages, a freshwater flux into the Mackenzie River outlet occurs without, but would be amplified by, drainage from Lake Agassiz during the YD (Tarasov et al., 2012).

Ice sheet response to climate forcing

Coupling the new chronological dataset with the North American ice-sheet model simulations of Tarasov et al. (2012) demonstrates a retreat pattern primarily driven by surface ablation and increased ice streaming to the ablation zones (Figs. 2 and 3D). Rapid succession of changing ice-stream orientations (Ross et al., 2009; Ó Cofaigh et al., 2010; Norris et al., 2017; Margold et al., 2018) provides geomorphic evidence of a rapidly evolving deglacial system. Numerical simulations indicate the SWLIS margin experienced initial rapid retreat of 380–340 m a−1 following CIS-LIS separation (after ca. 14.9 ka) until the YD (ca. 13.0 ka). Between ca. 13 and 11 ka, numerical modeling shows low retreat rates (≤160 m a−1) or ice-sheet stabilization in response to the YD cooling. Retreat rates are higher and more variable than contemporaneous rates observed in the southeastern LIS (e.g., Lowell et al., 2021). We suggest this reduction in

retreat rates is, in part, influenced by the LIS margin retreating to the Canadian Shield, which could support higher shear stresses at the ice-bed interface (Tarasov et al., 2012).

The more-rapid deglaciation of the Interior Plains, and the older age for the CLM as the SWLIS's YD position, results in retreat rates up to 60% higher than suggested by 14C-constrained margin chronologies (Dalton et al., 2020). More-rapid deglaciation of the SWLIS margin translates to a sea-level contribution of ~3.7 m in the 1700 yr of the B-A interval and a total contribution of ~5.7 m for the total retreat period. This response of the SWLIS parallels reconstruction of the CIS (Menounos et al., 2017), providing a growing body of evidence to support a rapid continental-wide response of the North American Ice Sheet Complex to B-A warming.

CONCLUSIONS

Chronological reconstruction using 10Be exposure ages in addition to preexisting 10Be exposure, luminescence, and minimum-limiting 14C dates presents an internally consistent retreat record for the SWLIS. These data demonstrate rapid deglaciation of the SWLIS contemporaneous with B-A warming. 10Be exposure ages establish the YD margin position that facilitated meltwater drainage to the Arctic from glacial Lake Agassiz. Direct dating from the CIS-LIS convergence zone to this position demonstrates the LIS retreated >1200 km from its coalescence with the CIS in ≤2500 years, reaching retreat rates of ~350 m a−1. Coupled with numerical modeling, these results suggest the SWLIS contributed ~3.7 m of sea-level rise during the B-A period. The rapid ice-margin retreat was followed by stabilization of LIS at the CLM during the YD..

ACKNOWLEDGMENTS

This research was funded by the Natural Sciences and Engineering Research Council of Canada (D.G. Froese, J.C. Gosse, and L. Tarasov) and the Canada Research Chair Program (D.G. Froese). Numerical simulations were completed using the ACEnet supercomputing cluster at Memorial University of Newfoundland. We thank G. Yang for BeO target chemistry; B. Menounos, J. England, A. Reyes, and N. Atkinson for comments on an early manuscript version; and D. Utting for suggesting erratic locations. This work was performed at Lawrence Livermore National Laboratory under contract DE-AC52-07NA27344. This is Lawrence Livermore National Laboratory contribution LLNL-JRNL-808330. We thank editor William Clyde and reviewers Martin Ross, James Teller, and an anonymous reviewer.

References

Borchers, B., Marrero, S., Balco, G., Caffee, M., Goehring, B., Lifton, N., Nishiizumi, K., Phillips, F., Schaefer, J., and Stone, J., 2016, Geological calibration of spallation production rates in the CRONUS-Earth project: Quaternary Geochronology, v. 31, p. 188–198, https://doi.org/10.1016/j.quageo.2015.01.009.

Bronk Ramsey, C., 2009, Bayesian analysis of radiocarbon dates: Radiocarbon, v. 51, p. 337–360, https://doi.org/10.1017/S0033822200033865.

Carlson, A.E., and Clark, P.U., 2012, Ice sheet sources of sea level rise and freshwaterdischarge during the last deglaciation: Reviews of Geophysics, v. 50, RG4007, https://doi .org/10.1029/2011RG000371.

Clark, P.U., and Tarasov, L., 2014, Closing the sea level budget at the Last Glacial Maximum: Proceedings of the National Academy of Sciences of the United States of America, v. 111, p. 15,861–15,862, https://doi.org/10.1073/pnas.1418970111.

Condron, A., and Winsor, P., 2012, Meltwater routing and the Younger Dryas: Proceedings of the National Academy of Sciences of the United States of America, v. 109, p. 19,928–19,933, https://doi .org/10.1073/pnas.1207381109.

Dalton, A.S., et al., 2020, An updated radiocarbon-based ice margin chronology for the last deglaciation of the North American Ice Sheet Complex: Quaternary Science Reviews, v. 234, 106223, https://doi.org/10.1016/j.quascirev.2020.106223.

Dyke, A.S., Moore, A., and Robertson, L., 2003, Deglaciation of North America: Geological Survey of Canada Open File 1574, 2 sheets, scale 1:30,000,000, 1 CD-ROM, https://doi .org/10.4095/214399.

Fisher, T.G., Waterson, N., Lowell, T.V., and Hajdas, I., 2009, Deglaciation ages and meltwater routing in the Fort McMurray region, northeastern Alberta and northwestern Saskatchewan, Canada: Quaternary Science Reviews, v. 28, p. 1608–1624, https://doi.org/10.1016/j.quascirev.2009.02.003.

Froese, D.G., Young, J.M., Norris, S.L., and Margold, M., 2019, Availability and viability of the ice-free corridor and Pacific coast routes for the peopling of the Americas: The SAA [Society for American Archaeology] Archaeological Record, v. 19, no. 3, p. 27–33.

Gregoire, L.J., Payne, A.J., and Valdes, P.J., 2012, Deglacial rapid sea level rises caused by ice-sheet saddle collapses: Nature, v. 487, p. 219–222, https://doi.org/10.1038/nature11257.

Gregoire, L.J., Otto-Bliesner, B., Valdes, P.J., and Ivanovic, R., 2016, Abrupt Bølling warming and ice saddle collapse contributions to the Meltwater Pulse 1a rapid sea level rise: Geophysical Research Letters, v. 43, p. 9130–9137, https://doi .org/10.1002/2016GL070356.

Heintzman, P.D., et al., 2016, Bison phylogeography constrains dispersal and viability of the Ice Free Corridor in western Canada: Proceedings of the National Academy of Sciences of the United States of America, v. 113, p. 8057–8063, https://doi.org/10.1073/pnas.1601077113.

Keigwin, L.D., Klotsko, S., Zhao, N., Reilly, B., Giosan, L., and Driscoll, N.W., 2018, Deglacial floods in the Beaufort Sea preceded Younger Dryas cooling: Nature Geoscience, v. 11, p. 599–604, https://doi.org/10.1038/s41561-018-0169-6.

Lambeck, K., Rouby, H., Purcell, A., Sun, Y., and Sambridge, M., 2014, Sea level and global ice volumes from the Last Glacial Maximum to the Holocene: Proceedings of the National Academy of Sciences of the United States of America, v. 111, p. 15296–15303, https://doi.org/10.1073/pnas.1411762111.

Lifton, N., Sato, T., and Dunai, T.J., 2014, Scaling *in situ* cosmogenic nuclide production rates using analytical approximations to atmospheric cosmic-ray fluxes: Earth and Planetary Science Letters, v. 386, p. 149–160, https://doi.org/10.1016/j.epsl.2013.10.052.

Lowell, T.V., Kelly, M.A., Howley, J.A., Fisher, T.G., Barnett, P.J., Schwartz, R., Zimmerman, S.R., Norris, N., and Malone, A.G., 2021, Near-constant retreat rate of a terrestrial margin of the Laurentide Ice Sheet during the last deglaciation: Geology, v. 49, https://doi.org/10.1130/G49081.1 (in press).

Margold, M., Stokes, C.R., and Clark, C.D., 2018, Reconciling records of ice streaming and ice margin retreat to produce a palaeogeographic reconstruction of the deglaciation of the Laurentide Ice Sheet: Quaternary Science Reviews, v. 189, p. 1–30, https://doi.org/10.1016/j.quasci-rev.2018.03.013.

Margold, M., Gosse, J.C., Hidy, A.J., Woywitka, R.J., Young, J.M., and Froese, D., 2019, Beryllium-10 dating of the Foothills Erratics Train in Alberta, Canada, indicates detachment of the Laurentide Ice Sheet from the Rocky Mountains at ~15 ka: Quaternary Research, v. 92, p. 469–482, https://doi.org/10.1017/qua.2019.10.

Menounos, B., et al., 2017, Cordilleran Ice Sheet mass loss preceded climate reversals near the Pleistocene Termination: Science, v. 358, p. 781–784, https://doi.org/10.1126/science.aan3001.

Munyikwa, K., Feathers, J.K., Rittenour, T.M., and Shrimpton, H.K., 2011, Constraining the Late Wisconsinan retreat of the Laurentide ice sheet from western Canada using luminescence ages from postglacial aeolian dunes: Quaternary Geochronology, v. 6, p. 407–422, https://doi.org/10.1016/j.quageo.2011.03.010.

Munyikwa, K., Rittenour, T.M., and Feathers, J.K., 2017, Temporal constraints for the Late Wisconsinan deglaciation of western Canada using eolian dune luminescence chronologies from Alberta: Palaeogeography, Palaeoclimatology, Palaeoecology, v. 470, p. 147–165, https://doi.org/10.1016/j.palaeo.2016.12.034.

Murton, J.B., Bateman, M.D., Dallimore, S.R., Teller, J.T., and Yang, Z., 2010, Identification of Younger Dryas outburst flood path from Lake Agassiz to the Arctic Ocean: Nature, v. 464, p. 740–743, https://doi.org/10.1038/nature08954.

Norris, S.L., Margold, M., and Froese, D.G., 2017, Glacial landforms of northwest Saskatchewan: Journal of Maps, v. 13, p. 600–607, https://doi .org/10.1080/17445647.2017.1342212.

Norris, S.L., Garcia-Castellanos, D., Jansen, J.D., Carling, P.A., Margold, M., Woywitka, R.J., and Froese, D.G., 2021, Catastrophic drainage from the northwestern outlet of glacial Lake Agassiz during the Younger Dryas: Geophysical Research Letters, v. 48, e2021GL093919, https://doi.org/10.1029/2021GL093919.

Ó Cofaigh, C., Evans, D.J.A., and Smith, I.R., 2010, Large-scale reorganization and sedimentation of terrestrial ice streams during late Wisconsinan Laurentide Ice Sheet deglaciation: Geological Society of America Bulletin, v. 122, p. 743–756, https://doi.org/10.1130/B26476.1.

Pedersen, M.W., et al., 2016, Postglacial viability and colonization in North America's ice-free corridor: Nature, v. 537, p. 45–49, https://doi.org/10.1038/nature19085.

Potter, B.A., et al., 2018, Current evidence allows multiple models for the peopling of the Americas: Science Advances, v. 4, eaat5473, https://doi .org/10.1126/sciadv.aat5473.

Rasmussen, S.O., et al., 2006, A new Greenland ice core chronology for the last glacial termination: Journal of Geophysical Research: Atmospheres, v. 111, D6, https://doi.org/10.1029/2005 JD006079.

Rasmussen, S.O., et al., 2014, A stratigraphic framework for abrupt climatic changes during the Last Glacial period based on three synchronized Greenland ice-core records: Refining and extending the INTIMATE event stratigraphy: Quaternary Science Reviews, v. 106, p. 14–28, https://doi.org/10.1016/j.quascirev.2014.09.007.

Ross, M., Campbell, J.E., Parent, M., and Adams, R.S., 2009, Palaeo-ice streams and the subglacial landscape mosaic of the North American mid-continental prairies: Boreas, v. 38, p. 421–439, https://doi.org/10.1111/j.1502-3885.2009.00082.x.

Smith, D.G., and Fisher, T.G., 1993, Glacial Lake Agassiz: The northwestern outlet and paleoflood: Geology, v. 21, p. 9–12, https://doi .org/10.1130/0091-7613(1993)021<0009:GLATNO>2.3.CO;2.

Tarasov, L., and Peltier, W.R., 2005, Arctic freshwater forcing of the Younger Dryas cold reversal: Nature, v. 435, p. 662–665, https://doi.org/10.1038/nature03617.

Tarasov, L., Dyke, A.S., Neal, R.M., and Peltier, W.R., 2012, A data-calibrated distribution of deglacial chronologies for the North American ice complex from glaciological modelling: Earth and Planetary Science Letters, v. 315, p. 30–40, https://doi.org/10.1016/j.epsl.2011.09.010.

Teller, J.T., Boyd, M., Yang, Z., Kor, P.S.G., and Fard, A.M., 2005, Alternative routing of Lake Agassiz overflow during the Younger Dryas: New dates, paleotopography, and a re-evaluation: Quaternary Science Reviews, v. 24, p. 1890–1905, https://doi .org/10.1016/j.quascirev.2005.01.008.

Wolfe, S.A., Huntley, D.J., and Ollerhead, J., 2004, Relict late Wisconsinan dune fields of the northern Great Plains, Canada: Géographie Physique et Quaternaire, v. 58, p. 323–336, https://doi .org/10.7202/013146ar.

Woywitka, R.J., 2019, Geoarchaeology of the mineable oil sands region, northeastern Alberta, Canada [Ph.D. thesis]: Edmonton, Canada, University of Alberta, 111 p., https://doi.org/10.7939/r3-t1nd-k544.

Young, J.M., Reyes, A.V., and Froese, D.G., 2020, Assessing the ages of the Moorhead and Emerson phases of glacial Lake Agassiz and their temporal connection to the Younger Dryas cold reversal: Quaternary Science Reviews, v. 251, 106714, https://doi.org/10.1016/j.quascirev.2020.106714.

FIGURE CAPTIONS

Figure 1. 10Be sample locations from Beaver River (BR), Clearwater Lower Athabasca Spillway (CLAS), Cree Lake Moraine (CLM), and the western and eastern upper Cree Lake Moraine (UCLM-W and UCLM-E) in the Interior Plains, Canada. Deglacial isochrones (presented in calibrated years B.P.) from ca. 19,000 to 11,400 ka are labeled in gray (after Dalton et al., 2020). Preexisting selected luminescence, 10Be exposure (using a LSDn production rate scaling and 0 mm of erosion rate correction), and 14C are grouped (sites A–Z, AA; sites within 40 km of each other are grouped). Ages included in Bayesian modeling are in white. Outliers are removed following the original authors or as explained in Table S3 in the Supplemental Material (see footnote 1), and average dates are indicated along with number of samples (*n*). Individual and site means (in bold) expressed using an error-weighted mean are displayed for newly acquired 10Be ages. CIS—Cordilleran Ice Sheet; LIS—Laurentide Ice Sheet; OSL—optically stimulated luminescence; IRSL—infrared stimulated luminescence.

Figure 2. Modeled ice margin retreat for the southwestern Laurentide Ice Sheet extent between 15 and 10 ka. Locations of 10Be exposure ages are in gray. BR—Beaver River; CLAS—Clearwater

Lower Athabasca Spillway; CLM—Cree Lake Moraine; UCLM-W, UCLM-E—western and eastern upper Cree Lake Moraine); FET—Foothills Erratics Train; CIS—Cordilleran Ice Sheet; LIS—Laurentide Ice Sheet.

Figure 3. Compiled chronologies, retreat rates, and sea-level equivalent relating to the southwestern Laurentide Ice Sheet (SWLIS). MWP-1a—Meltwater Pulse-1a; B-A—Bølling-Allerød; YD—Younger Dryas; OSL—optically stimulated luminescence; IRSL—infrared stimulated luminescence; FET—Foothills Erratics Train. (A) 10Be exposure, luminescence, and 14C chronologies listed vertically from bottom to top following direction of ice retreat. See Figure 1 for site locations. 10Be dates are reported with 1σ uncertainty combined with production rate uncertainty, luminescence dates at 1σ uncertainty using a LSDn production rate scaling and 0 mm of erosion rate correction, and 14C dates at 2σ uncertainty (see Table S3 [see footnote 1] for summary of dates). IFC—Ice Free Corridor. (B) Modeled age ranges at 2σ (bracketed age) and probability density functions of initial separation of Cordilleran Ice Sheet (CIS) and Laurentide Ice Sheet (LIS) and formation of Cree Lake Moraine. (C) Light gray line shows mean rate of deglaciation from model simulations using Tarasov et al. (2012); dashed dark gray line is from Dalton et al. (2020). (D) SWLIS cumulative sea-level equivalent (cum. SLE) between 18 and 11 ka from model simulations using Tarasov et al. (2012). (E) Global mean sea level relative to modern mean sea level (Lambeck et al., 2014). (F) δ18O record from North Greenland Ice Core Project (NGRIP) (Rasmussen et al., 2006).

421 **Figure 1:**

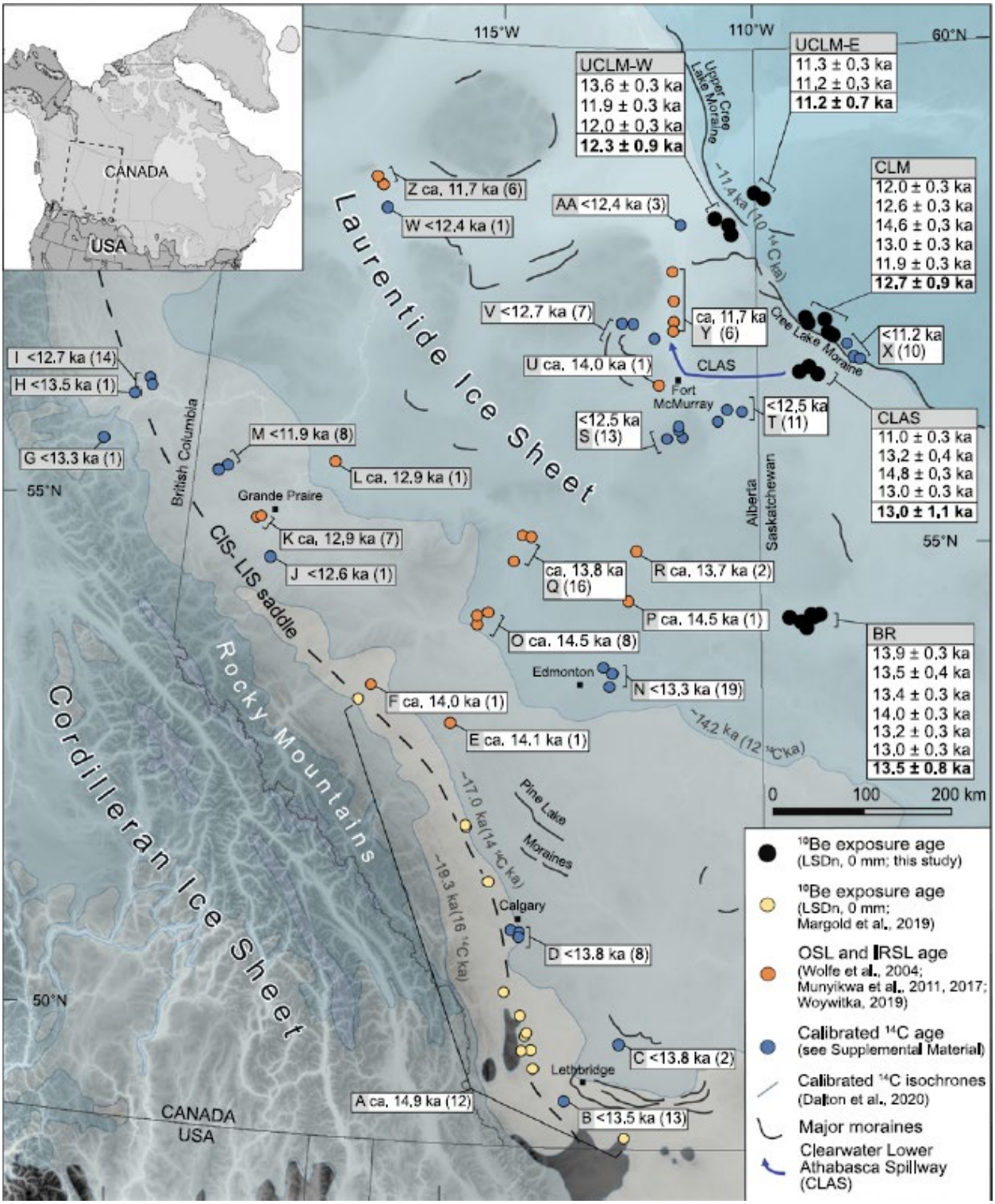

423

424

425 **Figure 2:**

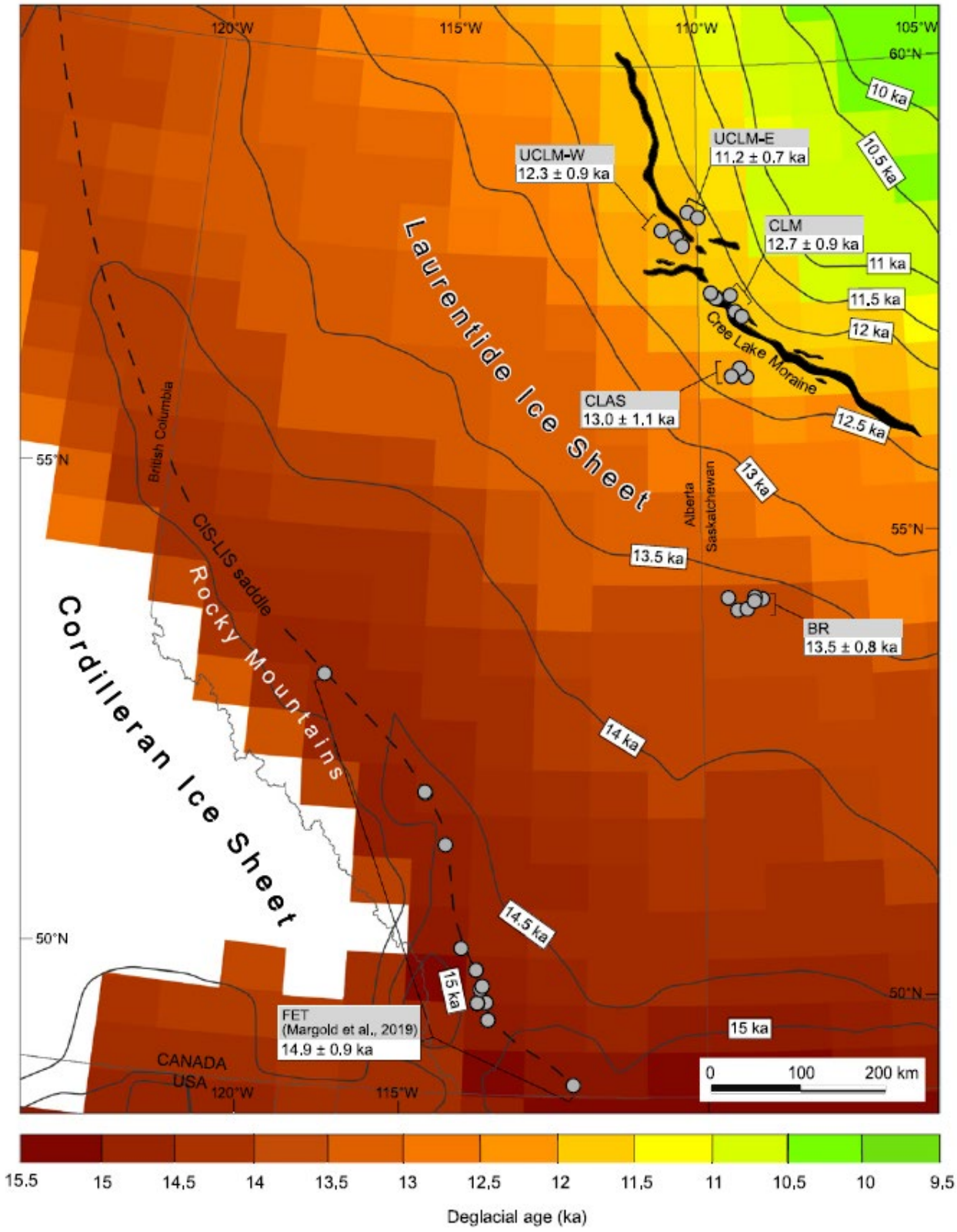
120°W
115°W
110°W
105°W
60°N
55°N
50°N
10 ka
10.5 ka
11 ka
11.5 ka
12 ka
12.5 ka
13 ka
13.5 ka
14 ka
14.5 ka
15 ka
UCLM-W
12.3 ± 0.9 ka
UCLM-E
11.2 ± 0.7 ka
CLM
12.7 ± 0.9 ka
Cree Lake Moraine
CLAS
13.0 ± 1.1 ka
BR
13.5 ± 0.8 ka
FET
(Margold et al., 2019)
14.9 ± 0.9 ka
Laurentide Ice Sheet
Cordilleran Ice Sheet
Rocky Mountains
CIS-LIS saddle
British Columbia
Alberta
Saskatchewan
CANADA
USA
0
100
200 km
15,5
15
14,5
14
13,5
13
12,5
12
11,5
11
10,5
10
9,5
Deglacial age (ka)

Figure 3:

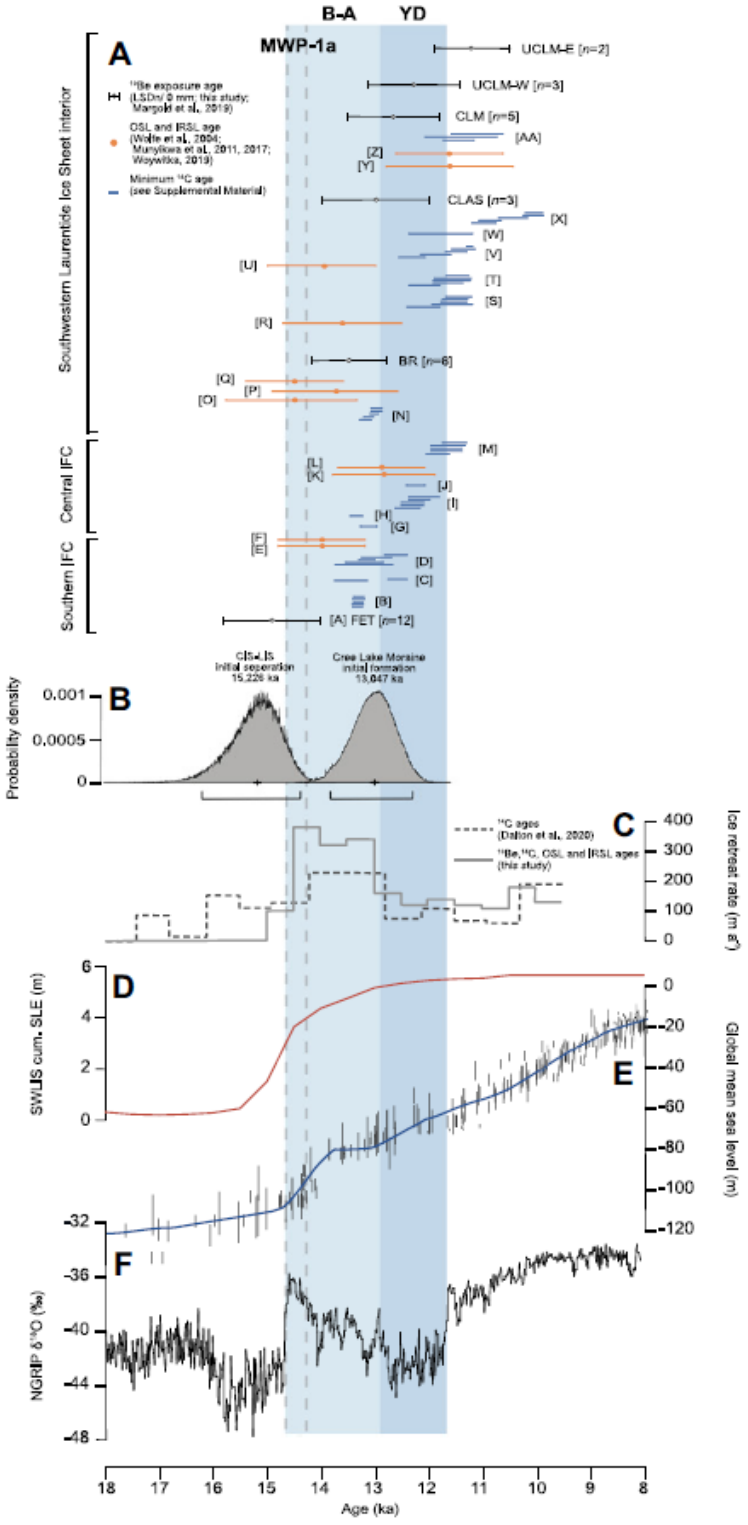
B-A
YD
MWP-1a
A
Southwestern Laurentide Ice Sheet interior
Central IFC
Southern IFC
UCLM-E [n=2]
UCLM-W [n=3]
CLM [n=5]
CLAS [n=3]
BR [n=6]
FET [n=12]
B
Probability density
CIS-LIS initial separation 15,226 ka
Cree Lake Moraine initial formation 13,047 ka
C
Ice retreat rate (m a⁻¹)
D
SWLIS cum. SLE (m)
E
Global mean sea level (m)
F
NGRIP δ¹⁸O (‰)
Age (ka)

SUPPLEMENTAL MATERIAL

Rapid retreat of the southwestern Laurentide Ice Sheet during the Bølling-Allerød interval

Sophie L. Norris, Lev Tarasov, Alistair J. Monteath, John C. Gosse, Alan J. Hidy, Martin Margold and Duane G. Froese
***Corresponding author: slnorris@ualberta.ca, duane.froese@ualberta.ca**

Methods

Cosmogenic nuclide exposure dating

Laboratory methods

26 boulder samples were collected for cosmogenic exposure dating using ^{10}Be at five site locations. These included: four from the Pine Lake Moraine (PLM), six from gravel bars within the Beaver River Spillway (BR), five from erosional residuals at the head of the Clearwater Athabasca Spillway (CLAS), five from the Cree Lake Moraine (CLM) and six from the western and eastern parts of the upper-Cree Lake Moraine (UCLM-W and UCLM-E). Samples reflect erosion residuals and gravel bars were formed by catastrophic outburst floods that drained, contemporaneous with ice retreat, from ice dammed lakes (see Norris et al., 2019, 2021). Samples were collected for exposure dating with a diamond blade cutoff saw or hammer and chisel. The sampled erratics consist of Precambrian rocks from the Athabasca Group sandstone and granites from the Canadian Shield. All samples were prepared as BeO targets at CRISDal Lab, Dalhousie University. To facilitate isolation of sufficient quartz, the following laboratory techniques were employed.

The samples were cleaned, crushed, and ground, and the 250-355 μm fraction was rinsed, leached in aqua regia (2 hours), and etched in HF, before mineral separation using combinations of froth floatation, Frantz magnetic separation, air abrasion, heavy liquids, and controlled digestions of non-quartz phases using hydrofluoric or hexafluorosilicic acids. When the quartz concentrate was sufficiently pure (as determined optically and with <100 ppm Al and Ti as determined on a 1 g aliquot with the lab's ICP-OES), approximately 35 wt% of the dried quartz concentrate was removed over three digestion-rinse cycles using an ultrasonic bath with dilute HF as per Kohl and Nishiizumi (1992). The samples were spiked with approximately 240 μg of

the lab's $BeCl_2$ carrier ('Be-Carrier-31-28Sept2012'; prepared from a deeply mined Ural Mountain phenacite with $^{10}Be/^{9}Be$ below 1 x 10^{-16}), and were digested in a $HF\text{-}HNO_3$ mixture, evaporated twice in perchloric acid, and treated with anion and cation column chemistry to isolate the Be^{2+}. After acidifying with perchloric and nitric acid to remove residual B, $Be(OH)_2$ was precipitated using ultrapure ammonia gas, transferred to a cleaned boron-free quartz vial and carefully calcined in a Bunsen burner flame to a white oxide for over three minutes. In an antistatic glovebox the BeO was powdered, mixed 2:3 by volume with high purity niobium powder (325 mesh), and packed into stainless steel cathodes for $^{10}Be/^{9}Be$ measurement at the Center for Accelerator Mass Spectrometry, Lawrence Livermore National Lab (CAMS-LLNL). These measurements were made against the 07KNSTD3110 standard with a known $^{10}Be/^{9}Be$ of $2850x10^{-15}$ (Nishiizumi et al. 2007). Process blanks were also analysed and used (average 1 blank per 8 samples) to subtract ^{10}Be introduced during target preparation and analysis. For all samples, this correction was less than 1% of the adjusted ^{10}Be values.

Age calculation

Exposure ages were calculated using the 'age calculator formerly known as CRONUS-Earth Online Exposure Age Calculator' (Balco et al., 2008; v3.0; constrants 3.0.3, at https://hess.ess.washington.edu/math/v3/v3_age_in.html) using the default calibration set of Borchers et al. (2016) and the time dependent 'LSDn' production scaling scheme of Lifton et al. (2014). Utilizing other scaling schemes or production rates does not alter our conclusions as the ages are within the internal uncertainty of our reported ages (Table DR1). Various factors control the cosmic ray flux to the boulder and therefore causing the calculated exposure ages to underestimate or overestimate the timing of ice marginal retreat at a site. Factors that will cause exposure ages to underestimate the age of retreat besides inheritance of cosmogenic ^{10}Be from exposure prior to deposition:

1. Snow and ice cover

The history of precipitation throughout the study area is uncertain, let alone the height and density of snow or ice cover which can be quite variable depending on local conditions (solar attitude, wind speed and direction, local and micro-topography, and vegetation). In the rain shadow of the Rocky Mountains, the study region currently has low winter

precipitation, and because the sampled boulder surfaces are mostly 0.5 m above ground level (mean=90 cm, median=82 cm, min=30 cm, max=160 cm above local ground level, only one boulder <50 cm), Table DR1) and situated on open plains or ridge tops, we would expect boulders to be windswept of snow or ice cover. Nevertheless, we tested the sensitivity of snow or ice shielding by using the climate normals data for a representative location inside the field area (Fort McMurray Airport, Alberta, 56.65°N, 111.22°W, 368 m asl) which has an elevation within 200 m of most samples (except for the Pine Lake moraine samples which are 926 m). The normals data indicate no month with an average snow depth >30 cm, although an extreme snow depth of 68 cm was recorded on Jan 2, 1968. Nevertheless, while most of the boulders are above that snow height, boulders would have still carried some snow cover. The mean snow depth is 25 cm in the four months with the greatest mean snow depth. Assuming that every boulder was covered by this amount for the four months every year since exposure began, and that the average snow density for the region is 0.224 gcm^{-3} (Williams, 1956), the shielding effect would be to decrease average ^{10}Be production rate by 3.66%. However, given the boulder height and exposed position of the boulders which would cause snow cover to be thinner and shorter, this is likely a significant overestimate, and the actual effect of snow or firn cover is less than 2%, i.e. the unadjusted exposure age could be an under-estimated by up to 2%. Wind speed and tree cover can also affect this estimate.

2. Tree shielding

The effect of tree shielding is difficult to estimate not only because it varies with time (and forest cover at each of the sample sites over the past 15 kyr is not certain), but it varies with forest density, forest type, fire frequency, and other factors (Plug et al., 2007). Plug et al. indicate that a temperate boreal forest may contribute as much as 2% shielding, and as most of the sample locations did not experience such a dense forest cover over the exposure duration (e.g. Ritchie, 1976) the average effect would likely be to underestimate the exposure age by < 1%.

3. Erosion

As indicated, the sampling strategy optimizes the collection of boulders with no evidence of erosion. Therefore, there may not have been any erosion. However, allowing for an average erosion rate for granitoid lithologies of 1 mm/kyr (Zimmerman et al., 1994; Blackwelder,

1978), and knowing the impact of erosion on exposure age will increase with exposure time, we compared the exposure ages calculated assuming both 0 and 1 mm/kyr. If the exposure history was adjusted for a 1 mm/kyr erosion rate, the exposure age would increase by an average of 1.0% (0.4% for the 6 kyr exposure, and 1.3% for the 16 kyr exposure). We cannot preclude that the boulders exhumed through some sediment cover (e.g. by frost heave or sediment erosion). However, because the boulders are relatively large and high, the terrain gently sloped, and the ages at each site relatively consistent and show no correlation with boulder height, we suggest that if boulder exhumation did occur it would have been early in the exposure history and not a significant impact on the ^{10}Be production history.

4. Atmospheric pressure changes

The mass of the atmosphere above a sample controls the energy spectrum and flux of secondary cosmic radiation to a boulder. Glacial isostatic adjustment (GIA) of the region, resulting from the depression of the lands surface by a >1.5 km thick continental ice sheet (Lambeck et al., 2017), affects the elevation and thus controls atmospheric thickness and secondary cosmic radiation shielding (Jones et al., 2017). Unlike snow or tree cover which have a large uncertainty owing to the lack of precise paleoclimate or paleovegetation data for each of the field areas, the is no doubt that some isostatic adjustment has occurred. The question is the magnitude and the change in the rate of surface uplift over the exposure history. As the study areas are not at the LGM limits of the LIS, post-glacial GIA here would mean that the production rate for the modern position of each boulder is overestimated and the exposure age is therefore underestimated. Correcting for a thicker atmospheric shielding early in the exposure history would therefore cause the adjusted ages to be slightly older, as with erosion or shielding. We apply a GIA correction using numerical model simulations of Tarasov et al. (2012) to determine the average elevation of the sample site since deglaciation. We calculate the elevation for each sample site at 1000 yr intervals, from ice free conditions within the model to 0 yrs, using dRSL data (Tarasov et al., 2012). Based on 1000 yr interval elevations we calculate a average dRSL for each sample site for this deglacial period. We then correct the modern elevation of our sample sites by the average deglacial dRSL elevation before the exposure age was calculated.

A GIA correction using alternative numerical model simulations (e.g. Lambeck et al., 2017; see Table DR1) display consistent results. The GIA-corrected exposure ages (e.g. Table SD1, $^{10}Be^{b}$) range from 8% to 3% older than the calculation without considering GIA ($^{10}Be^{a}$) depending on the exposure duration. While this is a significant systematic error, it is very ice-sheet model dependent, and ignores the many complex changes in atmospheric pressure related to katabatic winds off both ice sheets, changes in the density distribution of the atmosphere with global temperature, and more complex changes related to the impact of ice sheet geometry on atmospheric dynamics (Staiger et al., 2007). Using a global climate-model coupled with an ice sheet model, Staiger et al. (2007) showed that the atmospheric effect at high altitudes (Himalaya, ignoring GIA) would cause the production rate to be 6.5±1.5% greater during the LGM than today, but after the LGM the effect on time-integrated production rate would decrease and result in a total effect of 3% higher post-LGM time-integrated production rate than at that site today. The total effect at lower elevations and after the LGM such as this study will be less, but the complications related to the presence of ice sheets are difficult to assess. A further consideration is that while dRSL increments can be interpreted from various global datasets, the effect of a lower sea level and the displacement of atmosphere by ice sheets (Osmaston, 2005) also complicates the modeling of the atmospheric dynamics above land. Therefore, while the GIA adjustments may have contributed percent-level increases in the production rate of a boulder over time, the uncertainty in correcting time-average atmospheric shielding requires future effort to refine.

Compilation of pre-existing chronology

We compile a dataset of pre-existing luminescence, ^{10}Be surface exposure ages and 'high quality' minimum radiocarbon chronologies. Individual dates are summarised in Table 3.

Pre-existing ^{10}Be surface exposure ages are limited to a single study (Margold et al., 2019) in the region. 16 glacial erratic boulders that mark the zone of coalescence of the Laurentide and Cordilleran Ice Sheet have been recently re-dated (Margold et al., 2019) using ^{10}Be surface exposure ages. Of the 16 boulders dated, 12 accurately constrain the age of decoupling of the two ice sheets and are used by the original authors to provide a weighted mean age, including

propagated uncertainty, of 14,900 ± 900 cal yr BP. We present these dates at one standard deviation uncertainty consistent with our samples.

Optically stimulated luminescence (OSL) and infrared stimulated luminescence (IRSL), from eolian sands have been previously used to constrain deglaciation within the study region (Wolfe et al., 2004; Munyikwa et al., 2011, 2017). We collate dates and group them into sites within 30km and present the oldest reliable sites where several exist within a 40 km region. We remove outliers proposed by the original authors and present dates with one standard deviation uncertainty.

A large number of ^{14}C dates (see DR3) have been used to constrain the deglaciation of the southwestern sector of the LIS. We focus on 'high quality' minimum limiting ^{14}C chronologies and present the five oldest reliable dates from within a 40 km region. We exclude dates on bulk sediments, terrestrial shells or mixed assemblages. Where available Accelerator Mass Spectrometry (AMS) ^{14}C dates are prioritized over radiometric (conventual) dating methods. In cases of bone, ultrafiltered collagen samples, where available, are prioritized. We remove outliers proposed by the original authors or where later data complications make clear arguments for the exclusion of single unreproduced dates. Radiocarbon dates are recalibrated using the northern hemisphere IntCal20 calibration curve (Reimer et al., 2020) and presented at two standard deviation uncertainty.

Bayesian age modelling

We integrate luminescence dates (OSL/ IRSL), ^{10}Be exposure ages and ^{14}C dates within a Bayesian age model using OxCal v.4.4 (Bronk Ramsey, 2009a). The model uses the known sequence of ice-retreat, across the western Interior Plains (southwest-northeast demarcated by recessional moraines), as a 'prior model' and follows the sampling transect of cosmogenic ^{10}Be exposure dates from this study. The existing luminescence and five oldest ^{14}C-dates from a single landform, or within a 40 km region, are treated at site level similar to the cosmogenic data.

Within the *Sequence* model we place dates associated with the Foothills Erratics Train and the Cree Lake Moraine in continuous *Phases*, with no defined (stratigraphic or temporal) internal

order. We took this approach as the Foothills Erratics Train was sampled following the CIS/LIS saddle (Margold et al., 2019), while dates from the Cree Lake Moraine closely overlap and represent a prolonged still-stand. These *Phases* were separated by *Boundaries* which allowed us to quantify 'start' and 'end' dates for the Cree Lake Moraine emplacement (Bronk Ramsey, 2009a). Because ^{14}C ages do not directly date ice-retreat, but the age of organic carbon deposited an indeterminable amount of time after the ice has melted, ^{14}C dates were integrated into the model using the *Before* function which treats the data as minimum (*terminus ante quem*) age controls only. This approach was necessary as large numbers of comparatively precise ^{14}C dates could not be reconciled with luminescence and ^{10}Be exposure ages which were typically older than the ^{14}C measurements, and more closely date the timing of deglaciation.

Prior to model construction anomalous ^{14}C-dates from bulk sediments, terrestrial shells or mixed assemblages were manually excluded (see above) from the database and were not included in the *Sequence* model. A 'general' *Outlier_Model* was applied with a 5% chance of any date being an outlier. Statistical outliers that should be considered for rejection were identified using Agreement index values (<60%); however, dates were only removed if they reduced the overall Agreement Index of the model to below the recommended 60% threshold (Bronk Ramsey, 2009b). In practice, the manual filtering of anomalous data, treatment of ^{14}C dates as minimum ages and the large uncertainties associated with luminescence and ^{10}Be exposure ages meant that no dates needed to be removed from the Bayesian model.

Modelling of ice retreat and meltwater equivalent

We reran the two best-fitting North American ice-sheet model simulations of Tarasov et al. (2012) to estimate the rate of ice volume loss and equivalent sea level contribution from the SWLIS based on our new chronology. The original simulations were derived from an approximate Bayesian calibration of a glaciological model against a large set of geological and geophysical constraints. The model included 39 ensemble parameters that were calibrated to address uncertainties in climate forcing, basal drag, ice calving, and the amount of nudging towards the input target ice margin chronologies from Dyke (2004) (interpolated between available time-slices). The total amount of nudging is a part of the misfit score for the calibration and thereby the calibration endeavored to minimize the amount of nudging required. The

chronological acceleration of the target chronology was progressively increased from 21ka (calendar) to a maximum acceleration of 2.0 kyr (shifting the original 18.3 ka isochrone to 16.3 ka) then progressively relaxed to line back up at 9.28 ka. A mean ice sheet retreat rate was calculated using multiple transects, taken at 100 km intervals, perpendicular to ice retreat direction across the SWLIS. In order to further assess the connection between SWLIS ice retreat rates and rapid Bølling-Allerød warming a fully coupled ice/climate modelling should be applicated.

SUPPLEMENTAL REFERENCES

Balco, G., Stone, J. O., Lifton, N. A., and Dunai, T. J. 2008: A complete and easily accessible means of calculating surface exposure ages or erosion rates from ^{10}Be and ^{26}Al measurements. *Quaternary geochronology*, *3*(3), 174-195. https://doi.org/10.1016/j.quageo.2007.12.001

Benedict, J.B. 1993: Influence of snow upon rates of granodiorite weathering, Colorado Front Range, USA. *Boreas*, *22*(2), 87-92. https://doi.org/10.1111/j.1502-3885.1993.tb00167.x

Borchers, B., Marrero, S., Balco, G., Caffee, M., Goehring, B., Lifton, N., Nishiizumi, K., Phillips, F., Schaefer, J. and Stone, J. 2016: Geological calibration of sp ation production rates in the CRONUS-Earth project. *Quaternary Geochronology 31,* 188–198. https://doi.org/10.1016/j.quageo.2015.01.009

Bronk Ramsey, C., 2009a: Bayesian analysis of radiocarbon dates. *Radiocarbon*, 51(1), 337-360. https://doi.org/10.1017/S0033822200033865

Bronk Ramsey, C., 2009b: Dealing with outliers and offsets in radiocarbon dating. *Radiocarbon*, 51(3), 1023-1045. https://doi.org/10.1017/S0033822200034093

Jones, R.S., Whitehouse, P.L., Bentley, M.J., Small, D. and Dalton, A.S. 2019: Impact of glacial isostatic adjustment on cosmogenic surface-exposure dating. *Quaternary Science Reviews*, *212*, 206-212. https://doi.org/10.1016/j.quascirev.2019.03.012

Kohl, C. P., and Nishiizumi, K. 1992: Chemical isolation of quartz for measurement of in-situ-produced cosmogenic nuclides. *Geochimica et Cosmochimica Acta*, *56*(9), 3583-3587.
Lal, D. 1991: Cosmic ray labeling of erosion surfaces: in situ nuclide production. *Earth and Planetary Science Letters*, *104*, 424-439. https://doi.org/10.1016/0016-7037(92)90401-4

Lambeck, K., Purcell, A., and Zhao, S. 2017: The North American Late Wisconsin ice sheet and mantle viscosity from glacial rebound analyses. *Quaternary Science Reviews*, *158*, 172-210. https://doi.org/10.1016/j.quascirev.2016.11.033

Lifton, N., Sato, T., and Dunai, T. J. 2014: Scaling in situ cosmogenic nuclide production rates using analytical approximations to atmospheric cosmic-ray fluxes. *Earth and Planetary Science Letters*, *386*, 149-160. https://doi.org/10.1016/j.epsl.2013.10.052

Margold, M., Gosse, J. C., Hidy, A. J., Woywitka, R. J., Young, J. M. and Froese, D. 2019: Beryllium-10 dating of the Foothills Erratics Train in Alberta, Canada, indicates detachment of the Laurentide Ice Sheet from the Rocky Mountains at ~15 ka. *Quaternary Research, 92*(2), 469-482. https://doi.org/10.1017/qua.2019.10

Munyikwa, K., Feathers, J. K., Rittenour, T. M., and Shrimpton, H. K. 2011: Constraining the Late Wisconsinan retreat of the Laurentide ice sheet from western Canada using luminescence ages from postglacial aeolian dunes. *Quaternary Geochronology*, *6*(3-4), 407-422. https://doi.org/10.1016/j.quageo.2011.03.010

Munyikwa, K., Rittenour, T. M., and Feathers, J. K. 2017: Temporal constraints for the Late Wisconsinan deglaciation of western Canada using eolian dune luminescence chronologies from Alberta. *Palaeogeography, palaeoclimatology, palaeoecology*, *470*, 147-165. https://doi.org/10.1016/j.palaeo.2016.12.034

Nishiizumi, K., Imamura, M., Caffee, M. W., Southon, J. R., Finkel, R. C., and McAninch, J. 2007: Absolute calibration of ^{10}Be AMS standards. *Nuclear Instruments and Methods in Physics Research Section B: Beam Interactions with Materials and Atoms*, *258*(2), 403-413. https://doi.org/10.1016/j.nimb.2007.01.297

Osmaston, H.A., 2006. Should Quaternary sea-level changes be used to correct glacier ELAs, vegetation belt altitudes and sea level temperatures for inferring climate changes? Quaternary Research, *65(2)*, 244-251. https://doi.org/10.1016/j.yqres.2005.11.004

Peltier, W.R., Argus, D.F. and Drummond, R. 2015: Space geodesy constrains ice-age terminal deglaciation: the global ICE-6G_C (VM5a) model. *Journal of Geophysical Research, 120,* 450-487. https://doi.org/10.1002/2014JB011176

Plug, L.J., Gosse, J.C., McIntosh, J.J. and Bigley, R. 2007: Attenuation of cosmic ray flux in temperate forest. *Journal of Geophysical Research: Earth Surface*, *112*(F2). https://doi.org/10.1029/2006JF000668

Reimer, P.J., Austin, W.E.N., Bard, E. and Ramsey, C. 2020: The IntCal20 Northern Hemisphere radiocarbon age calibration curve (0-55 kcal BP). *Radiocarbon 62*(4). https://doi.org/10.1017/RDC.2020.41

Ritchie, J.C. 1976: The late-Quaternary vegetational history of the western interior of Canada. *Canadian Journal of Botany*, *54*(15), 1793-1818. https://doi.org/10.1139/b76-194

Staiger, J., Gosse, J., Toracinta, R., Oglesby, B., Fastook, J. and Johnson, J.V. 2007: Atmospheric scaling of cosmogenic nuclide production: climate effect. *Journal of Geophysical Research: Solid Earth*, *112*(B2). https://doi.org/10.1029/2005JB003811

Tarasov, L., Dyke, A.S., Neal, R.M. and Peltier, W.R. 2012: A data-calibrated distribution of deglacial chronologies for the North American ice complex from glaciological modelling. *Earth and Planetary Science Letters 315*, 30-40. https://doi.org/10.1016/j.epsl.2011.09.010

Williams, G.P. 1956 Study of snow density across Canada. NRCan Publication, 1956-08-01.

Wolfe, S., Huntley, D., and Ollerhead, J. 2004: Relict late Wisconsinan dune fields of the northern Great Plains, Canada. *Géographie physique et Quaternaire*, *58*(2-3), 323-336. https://doi.org/10.7202/013146ar

Zimmerman, S.G., Evenson, E.B., Gosse, J.C. and Erskine, C.P. 1994: Extensive boulder erosion resulting from a range fire on the type-Pinedale moraines, Fremont Lake, Wyoming. *Quaternary Research*, *42*(3), 255-265. https://doi.org/10.1006/qres.1994.1076

Figure S1. Photographs of boulders sampled for 10Be surface exposure ages.

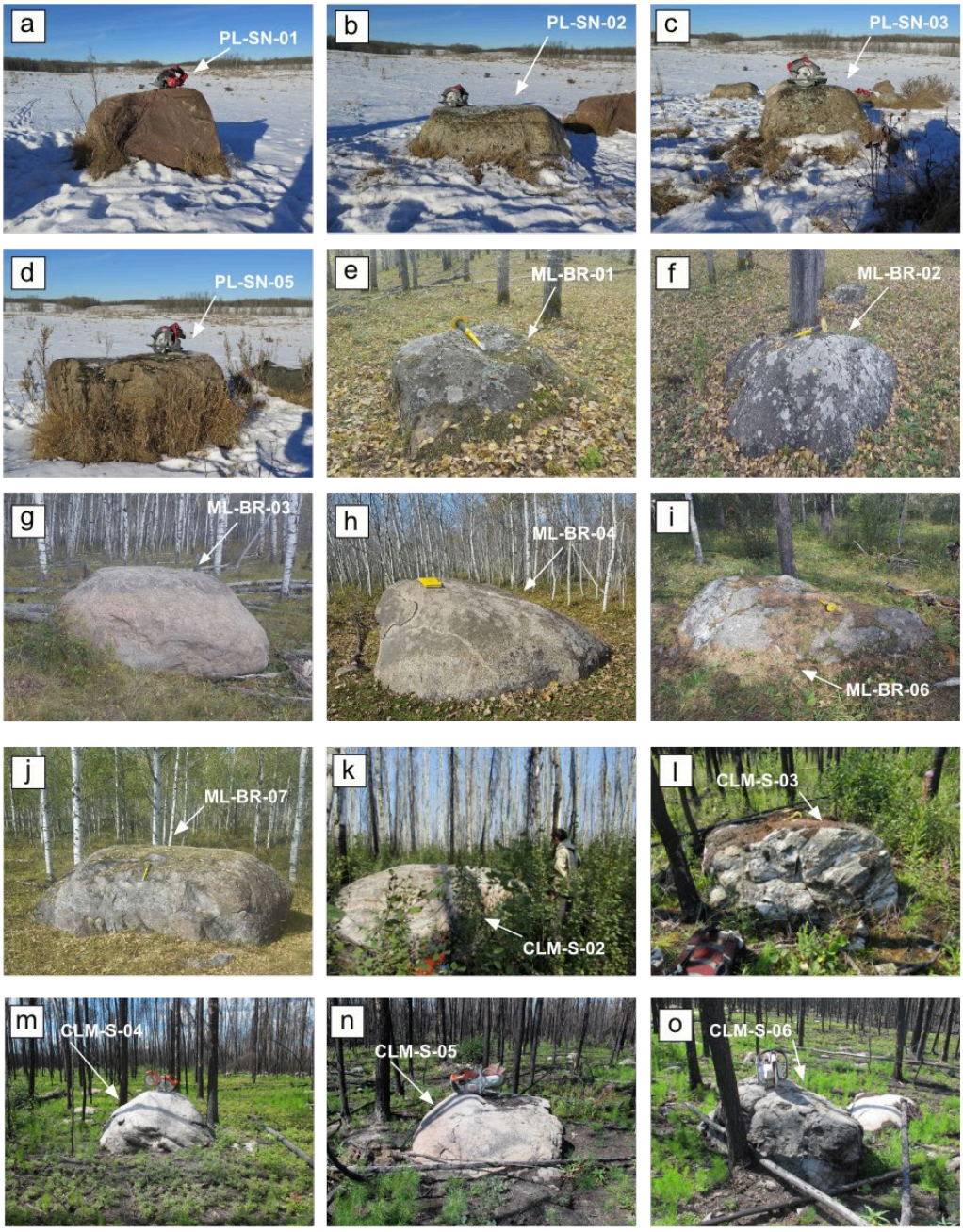


p
CLM-Mr-01
q
CLM-Mr-03
r
CLM-Mr-04
s
CLM-Mr-05
t
CLM-Mr-13
u
UCLM-E-03
v
UCLM-E-04
w
UCLM-E-05
x
UCLM-W-06
y
UCLM-W-07
z
UCLM-W-08

Figure S2. Probability density functions (i.e. 'normal kernel density estimate') for all ^{10}Be surface exposure samples sites. Blue lines represent reported age and 1 SD uncertainty, black lines are summed probabilities. Vertical black line represents the mean and grey boxes 1 SD excluding outliers of each sample site. Average ages, in bold, with propagated uncertainly calculated using the default calibration set of Borchers et al. (2016) and the time dependent 'LSDn' production scaling scheme of Lifton et al. (2014), with no correction for snow shielding and a zero erosion rate.

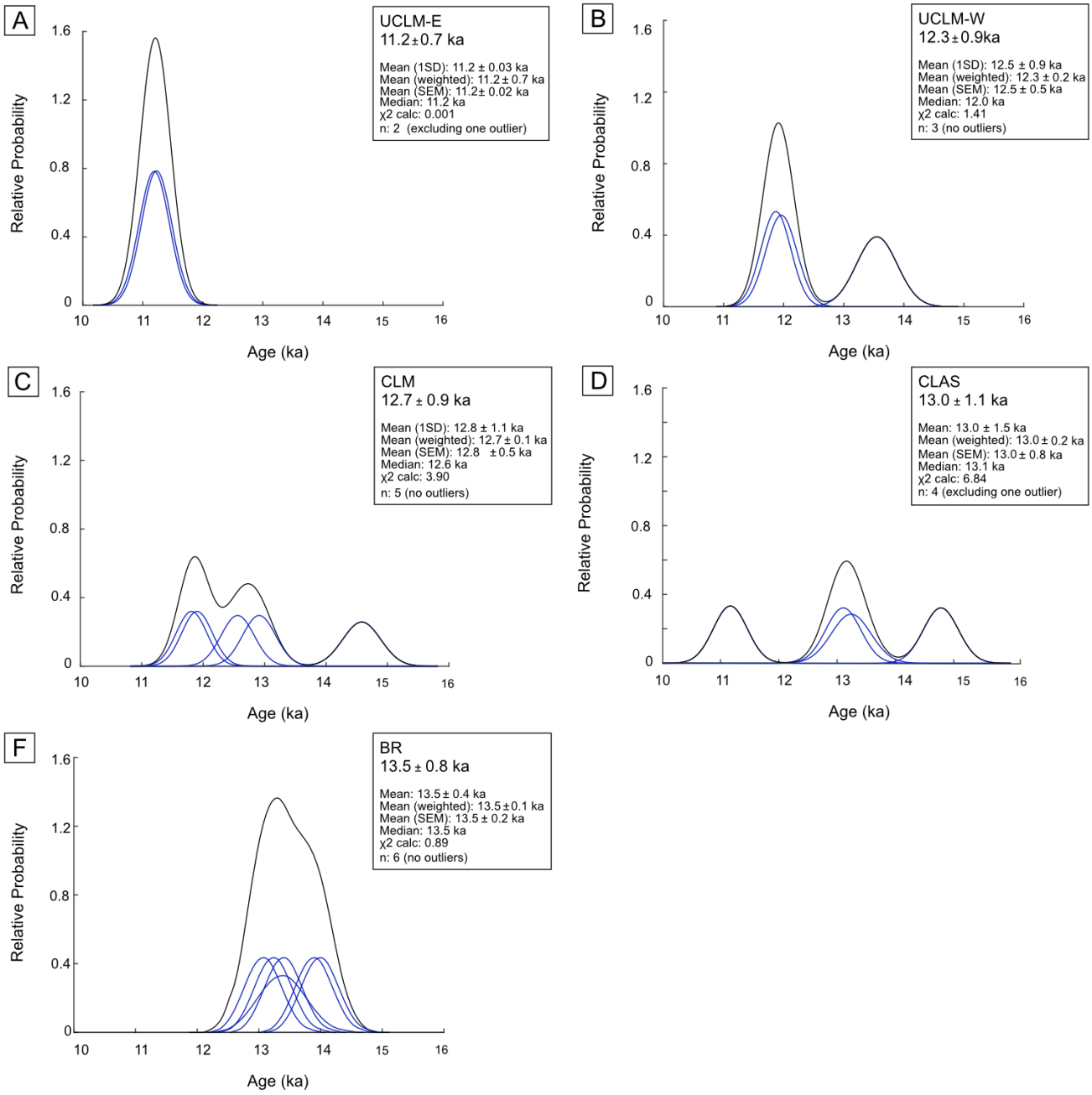

Figure S3. Bayesian age model output from OxCal v.4.4 (Bronk Ramsey, 2009a), using the IntCal20 calibration curve (Reimer et al., 2020) applied to the manually vetted radiocarbon, luminescence, and cosmogenic ages from the southwestern Laurentide Ice Sheet. The unmodelled (likelihood) probabilities are light grey, with modelled (posterior) probabilities in dark grey. Thick bar underlying the probability distributions is the 2-sigma confidence interval. Agreement indices (A:x) show probability of individual dates agreeing with the model.

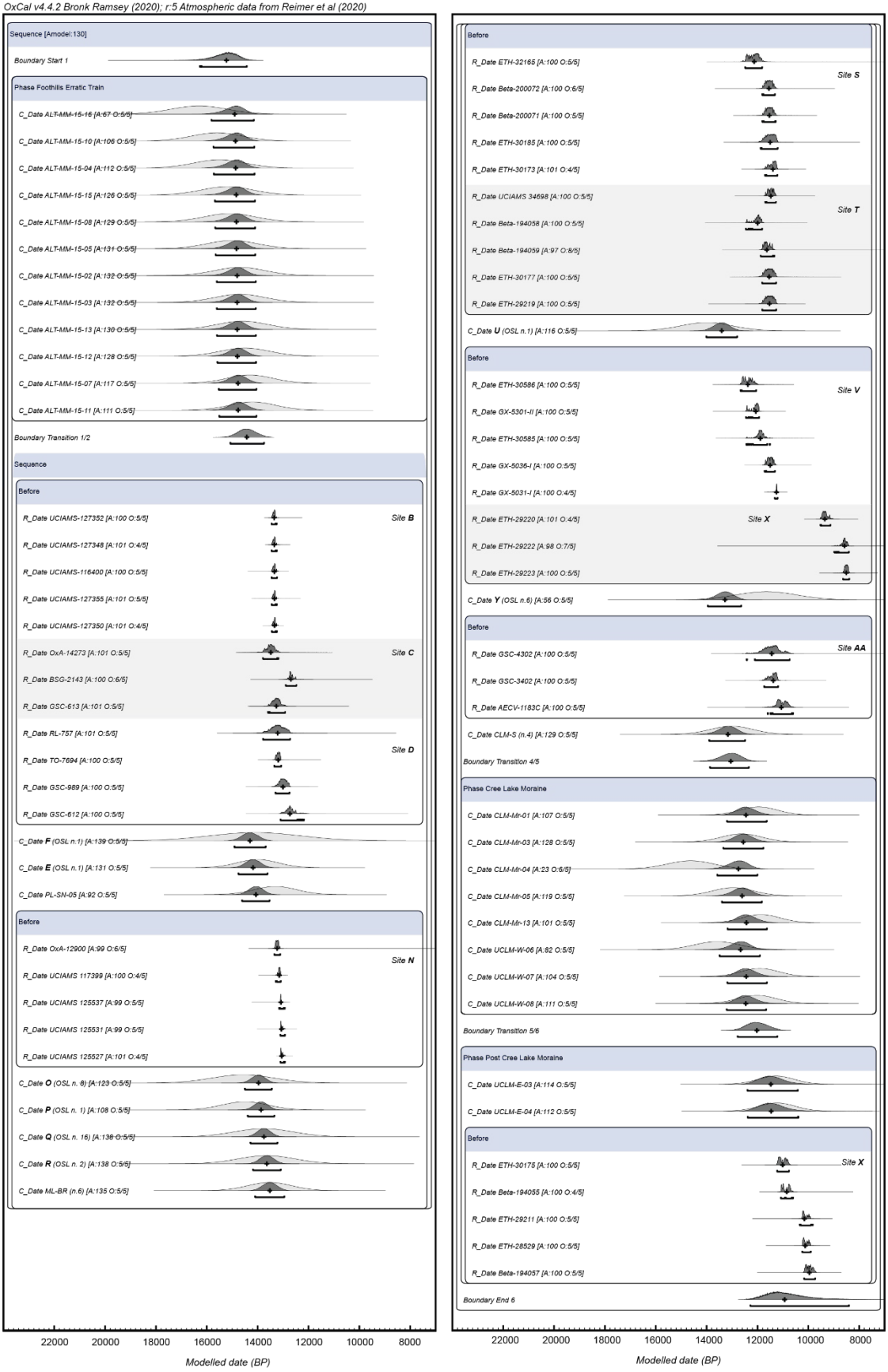
OxCal v4.4.2 Bronk Ramsey (2020); r:5 Atmospheric data from Reimer et al (2020)
Sequence [Amodel:130]
Boundary Start 1
Phase Foothills Erratic Train
C_Date ALT-MM-15-16 [A:67 O:5/5]
C_Date ALT-MM-15-10 [A:106 O:5/5]
C_Date ALT-MM-15-04 [A:112 O:5/5]
C_Date ALT-MM-15-15 [A:126 O:5/5]
C_Date ALT-MM-15-08 [A:129 O:5/5]
C_Date ALT-MM-15-05 [A:131 O:5/5]
C_Date ALT-MM-15-02 [A:132 O:5/5]
C_Date ALT-MM-15-03 [A:132 O:5/5]
C_Date ALT-MM-15-13 [A:130 O:5/5]
C_Date ALT-MM-15-12 [A:128 O:5/5]
C_Date ALT-MM-15-07 [A:117 O:5/5]
C_Date ALT-MM-15-11 [A:111 O:5/5]
Boundary Transition 1/2
Sequence
Before
R_Date UCIAMS-127352 [A:100 O:5/5]
Site B
R_Date UCIAMS-127348 [A:101 O:4/5]
R_Date UCIAMS-116400 [A:100 O:5/5]
R_Date UCIAMS-127355 [A:101 O:5/5]
R_Date UCIAMS-127350 [A:101 O:4/5]
R_Date OxA-14273 [A:101 O:5/5]
Site C
R_Date BSG-2143 [A:100 O:6/6]
R_Date GSC-613 [A:101 O:5/5]
R_Date RL-757 [A:101 O:5/5]
Site D
R_Date TO-7694 [A:100 O:5/5]
R_Date GSC-989 [A:100 O:5/5]
R_Date GSC-612 [A:100 O:5/5]
C_Date F (OSL n.1) [A:139 O:5/5]
C_Date E (OSL n.1) [A:131 O:5/5]
C_Date PL-SN-05 [A:92 O:5/5]
Before
R_Date OxA-12900 [A:99 O:6/6]
Site N
R_Date UCIAMS 117399 [A:100 O:4/5]
R_Date UCIAMS 125537 [A:99 O:5/5]
R_Date UCIAMS 125531 [A:99 O:5/5]
R_Date UCIAMS 125527 [A:101 O:4/5]
C_Date O (OSL n. 8) [A:123 O:5/5]
C_Date P (OSL n. 1) [A:108 O:5/5]
C_Date Q (OSL n. 16) [A:136 O:5/5]
C_Date R (OSL n. 2) [A:138 O:5/5]
C_Date ML-BR (n.6) [A:135 O:5/5]
22000
20000
18000
16000
14000
12000
10000
8000
Modelled date (BP)
Before
R_Date ETH-32165 [A:100 O:5/5]
Site S
R_Date Beta-200072 [A:100 O:6/5]
R_Date Beta-200071 [A:100 O:5/5]
R_Date ETH-30185 [A:100 O:5/5]
R_Date ETH-30173 [A:101 O:4/5]
R_Date UCIAMS 34698 [A:100 O:5/5]
Site T
R_Date Beta-194058 [A:100 O:5/5]
R_Date Beta-194059 [A:97 O:8/5]
R_Date ETH-30177 [A:100 O:5/5]
R_Date ETH-29219 [A:100 O:5/5]
C_Date U (OSL n.1) [A:116 O:5/5]
Before
R_Date ETH-30586 [A:100 O:5/5]
Site V
R_Date GX-5301-II [A:100 O:5/5]
R_Date ETH-30585 [A:100 O:5/5]
R_Date GX-5036-I [A:100 O:5/5]
R_Date GX-5031-I [A:100 O:4/5]
R_Date ETH-29220 [A:101 O:4/5]
Site X
R_Date ETH-29222 [A:98 O:7/5]
R_Date ETH-29223 [A:100 O:5/5]
C_Date Y (OSL n.6) [A:56 O:5/5]
Before
R_Date GSC-4302 [A:100 O:5/5]
Site AA
R_Date GSC-3402 [A:100 O:5/5]
R_Date AECV-1183C [A:100 O:5/5]
C_Date CLM-S (n.4) [A:129 O:5/5]
Boundary Transition 4/5
Phase Cree Lake Moraine
C_Date CLM-Mr-01 [A:107 O:5/5]
C_Date CLM-Mr-03 [A:128 O:5/5]
C_Date CLM-Mr-04 [A:23 O:6/5]
C_Date CLM-Mr-05 [A:119 O:5/5]
C_Date CLM-Mr-13 [A:101 O:5/5]
C_Date UCLM-W-06 [A:82 O:5/5]
C_Date UCLM-W-07 [A:104 O:5/5]
C_Date UCLM-W-08 [A:111 O:5/5]
Boundary Transition 5/6
Phase Post Cree Lake Moraine
C_Date UCLM-E-03 [A:114 O:5/5]
C_Date UCLM-E-04 [A:112 O:5/5]
Before
R_Date ETH-30175 [A:100 O:5/5]
Site X
R_Date Beta-194055 [A:100 O:4/5]
R_Date ETH-29211 [A:100 O:5/5]
R_Date ETH-28529 [A:100 O:5/5]
R_Date Beta-194057 [A:100 O:5/5]
Boundary End 6
22000
20000
18000
16000
14000
12000
10000
8000
Modelled date (BP)

Table S1. Cosmogenic ^{10}Be sample details and modelled surface exposure ages

Laboratory no.	Sample ID	Latitude (DD)	Longitude (DD)	Modern elevation (m a.s.l.)	Palaeo-elevation (m a.s.l.)[a]	Palaeo-elevation (m a.s.l.)[b]	Boulder height (m)	Sample thickness (cm)	Quartz Mass (g)	Be carrier mass (g)	$^{10}Be/^{9}Be$ (10^{-14})	$^{10}Be \pm 1\sigma$ (atoms g^{-1} SiO_2)	^{10}Be age[c] (ka)	10Be age[d] (ka)	^{10}Be age[e] (ka)
JG3829	PL-SN-01*	52.1622	-113.5128	927	890	898	0.7	2	20.2010	0.2504	6.56	56602 ± 1607	5.8 ± 0.2	6.0 ± 0.2	6.0 ± 0.2
JG3830	PL-SN-02*	52.1622	-113.5127	927	890	898	0.8	2	20.0614	0.2103	7.51	54769 ± 1976	5.7 ± 0.2	5.8 ± 0.2	5.9 ± 0.2
JG3831	PL-SN-03*	52.1621	-113.5127	926	889	897	1.6	2	25.0204	0.8262	13.16	80616 ± 1695	8.3 ± 0.2	8.5 ± 0.2	8.4 ± 0.2
JG3832	PL-SN-05*	52.1607	-113.5440	976	939	951	0.8	2	25.1980	0.8199	21.60	130685 ± 2587	12.9 ± 0.3	13.3 ± 0.3	13.3 ± 0.3
JG3826	ML-BR-01	54.2769	-109.0520	496	464	470	0.7	3	20.0280	0.208	12.48	90900 ± 2205	13.5 ± 0.3	13.9 ± 0.3	13.9 ± 0.3
JG3827	ML-BR-02	54.2770	-109.0521	492	460	467	0.8	2.5	20.0498	0.2109	11.93	88020 ±2402	13.1 ± 0.4	13.5 ± 0.4	13.5 ± 0.4
JG3612	ML-BR-03	54.2769	-109.0535	492	460	467	1	3	30.0720	0.2087	17.78	87398 ± 1848	13.1 ± 0.3	13.5 ± 0.3	13.4 ± 0.3
JG3613	ML-BR-04	54.2768	-109.0540	501	469	476	1.3	3	27.6640	0.1994	18.03	92033 ± 1943	13.6 ± 0.3	14.1 ± 0.3	14.0 ± 0.3
JG3614	ML-BR-06	54.3168	-109.5247	490	458	469	1	3	20.2070	0.212	12.04	85866 ± 1965	12.9 ± 0.3	13.2 ± 0.3	13.2 ± 0.3
JG3828	ML-BR-07	54.3179	-109.5248	526	494	502	1.6	3	20.0501	0.211	11.85	87450 ±2179	12.7 ± 0.3	13.0 ± 0.3	13.0 ± 0.3
JG3602	CLM-S-02	56.8340	-109.0767	455	401	408	0.8	2.5	15.2180	0.206	11.62	106578 ± 2095	16.3 ± 0.3	17.1 ± 0.3	16.9 ± 0.3
JG3603	CLM-S-03	56.8344	-109.0761	457	403	413	0.7	3.5	20.2939	0.2065	9.71	69762 ± 1890	10.7 ± 0.3	11.2 ± 0.3	11.1 ± 0.3
JG3604	CLM-S-04	56.9179	-108.9774	432	376	382	1	3	20.2990	0.2064	11.24	80821 ± 2165	12.6 ± 0.3	13.3 ± 0.4	13.2 ± 0.4
JG3605	CLM-S-05*	56.9178	-108.9780	425	369	373	0.5	2	27.6148	0.2134	16.56	90659 ± 1910	14.2 ± 0.3	15.0 ± 0.3	14.8 ± 0.3
JG3606	CLM-S-06	56.9179	-108.9780	425	369	373	0.5	2.5	20.1880	0.2070	10.99	79711 ± 1897	12.5 ± 0.3	13.2 ± 0.3	13.0 ± 0.3
JG3607	CLM-Mr-01	57.5234	-109.3115	566	497	510	1.2	1.5	30.0719	0.2141	16.63	83839 ± 1766	11.4 ± 0.3	12.1 ± 0.3	12.0 ± 0.3
JG3608	CLM-Mr-03	57.5233	-109.3106	569	500	515	0.7	1.5	27.5660	0.2022	17.04	88465 ± 1866	12.0 ± 0.3	12.8 ± 0.3	12.6 ± 0.3
JG3609	CLM-Mr-04	57.3490	-109.2239	554	493	507	0.5	2	20.2944	0.2059	14.08	101095 ± 2170	14 .0 ± 0.3	14.8 ± 0.3	14.6 ± 0.3
JG3610	CLM-Mr-05	57.3500	-109.2241	562	501	515	0.5	1.5	30.0501	0.2067	18.61	90668 ± 1868	12.4 ± 0.3	13.1 ± 0.3	13.0 ± 0.3
JG3611	CLM-Mr-13	57.5237	-109.3104	573	504	514	0.3	2	30.1446	0.2076	17.11	83457 ± 1758	11.3 ± 0.2	12.1 ± 0.3	11.9 ± 0.3
JG3615	UCLM-E-03	58.4685	-110.1993	285	207	217	1.6	4	27.5495	0.1992	11.59	59225 ± 1336	10.7 ± 0.2	11.6 ± 0.3	11.3 ± 0.3
JG3616	UCLM-E-04	58.4688	-110.2001	281	203	216	1	4	30.0464	0.2061	12.12	58797 ± 1336	10.7 ± 0.2	11.6 ± 0.3	11.2 ± 0.3
JG3617	UCLM-E-05*	58.4678	-110.1981	283	205	218	1.3	4	27.5301	0.2004	16.15	83232 ± 1761	15.1 ± 0.3	16.3 ± 0.3	16.0 ± 0.3

JG3618	UCLM-W-06	58.1798	-110.4310	315	250	263	0.6	4	30.0209	0.2088	14.99	73800 ± 1839	13.0 ± 0.3	13.9 ± 0.3	13.6 ± 0.3
JG3619	UCLM-W-07	58.1807	-110.4298	344	279	288	1	4	27.5892	0.2035	12.82	66875 ± 1412	11.4 ± 0.2	12.2 ± 0.3	11.9 ± 0.3
JG3620	UCLM-W-08	58.1807	-110.4296	335	270	279	1.3	4	27.5556	0.2132	12.22	66859 ± 1432	11.5 ± 0.2	12.3 ± 0.3	12.0 ± 0.3

Notes: Rock density for all samples is 2.6 g cm^{-3}; no shielding correction applied to samples; exposure ages were calculated using the online calculator formerly known as CRONUS (Balco et al., 2008; v3.0; constants 3.0.3)

*Statistical outliers excluded from site mean ages

[a] Palaeo-elevation derived using a GIA correction using numerical model simulations of Tarasov et al. (2012)

[b] Palaeo-elevation derived using a GIA correction using numerical model simulations of Lambeck et al. (2017)

[c] Ages (reported with 1σ internal error), calculated using the CRONUS default production rate (Borchers et al., 2016), Lm scaling (Lal, 1991/Stone, 2000) and modern-day elevations

[d] Ages (reported with 1σ internal error), calculated using the CRONUS default production rate (Borchers et al., 2016), Lm scaling (Lal, 1991/Stone, 2000) and glacioisostatic palaeo-elevations.

[e] Ages (reported with 1σ internal error), calculated using the CRONUS default production rate (Borchers et al., 2016), LSDn scaling (Lifton et al., 2014) and glacioisostatic palaeo-elevations.

Table S2. Summary statistics for ^{10}Be surface-exposure age distributions

Data Set	*N*	$N_{removed}$	Mean age (ka)	±1σ (ka)	Propagated uncertainty (ka)	Error-weighted mean (ka)	Standard error of the weighted mean (ka)	Weighted standard deviation (ka)	Median age (ka)	χ^2 calculated	χ^2 expected (95%)	χ^2 test (Pass/Fail)
UCLM-E (outliers)	3	-	12.8	2.7	1.6	12.3	0.2	1.6	11.3	11.64	5.99	Fail
UCLM-E (no outliers)	2	1	11.2	0.03	0.7	11.2	0.2	0.02	11.2	0.001	3.84	Pass
UCLM-W (no outliers)	3	-	12.5	0.9	0.9	12.3	0.2	0.5	12.0	1.41	5.99	Pass
CLM (no outliers)	5	-	12.8	1.1	0.9	12.7	0.1	0.5	12.6	3.90	9.49	Pass
CLAS (outliers)	5	-	13.8	2.2	1.3	13.7	0.1	1.0	13.2	13.90	9.49	Fail
CLAS (no outliers)	4	1	13.0	1.5	1.1	13.0	0.2	0.8	13.1	6.84	7.82	Pass
BR (no outliers)	6	-	13.5	0.4	0.8	13.5	0.1	0.2	13.5	0.89	11.07	Pass